Annu. Rev. Nucl. Part. Sci. 1991. 41: 97–132

HADRON COLLIDER PHYSICS[1]

Marjorie D. Shapiro

Lawrence Berkeley Laboratory, Berkeley, California 94720

James L. Siegrist

SSC Laboratory, Dallas, Texas 75237

KEY WORDS: QCD, electroweak, heavy flavor, jet production, W and Z bosons, top quark

CONTENTS

[1] This work was supported by the Office of Energy Research, Office of High Energy and Nuclear Physics, Division of High Energy Physics of the US Department of Energy under Contract DE-AC03-76SF00098.

0163–8998/91/1201–0097$02.00

Hadron colliders provide an important laboratory for testing the Standard Model of strong and electroweak interactions. Because such colliders have the highest available center-of-mass energy ($\sqrt{s}$), they probe the shortest accessible length scales and hence provide a unique opportunity both to study the fundamental fields of the Standard Model and to search for deviations from the predictions of the Standard Model. We present here recent results in the field of experimental hadron collider physics.

1. PHENOMENOLOGICAL OVERVIEW

1.1 *Particle Production in Soft Processes*

The total $p\bar{p}$ cross section, σ_{tot}, is dominated by soft processes. Because most $p\bar{p}$ interactions involve low momentum transfers, it is not possible to calculate the total cross section using perturbative quantum chromodynamics (QCD). Instead, it is necessary to parametrize σ_{tot} phenomenologically. The models used to describe the features of soft hadronic interactions share two common features (1). First, because the momentum transfer in most collisions is small, particles are produced with limited transverse momentum (p_t) with respect to the incoming $p\bar{p}$ direction. Second, because there are no severe dynamical constraints in the problem, the particles have a distribution of longitudinal momenta with respect to the beamline ($p_\parallel$) that is determined chiefly by the available phase space.

The three-dimensional phase-space element can be expressed in terms of p_t and $p_\parallel$:

$$\frac{d^3p}{E} = d\phi \frac{dp_t^2}{2} \frac{dp_\parallel}{E}, \qquad 1.$$

where ϕ is the azimuthal angle. Hence the invariant single-particle cross section can be written

$$E\frac{d\sigma}{d^3p} = \frac{1}{\pi} \frac{d\sigma}{dp_t^2\, dy}, \qquad 2.$$

where we have integrated over azimuth and where the rapidity y is defined as

$$y \equiv \frac{1}{2} \ln\left(\frac{E+p_\parallel}{E-p_\parallel}\right) \qquad 3.$$

so that $dy = dp_\parallel/E$. In the case where particle masses can be neglected, $y \approx -\ln[\tan(\theta/2)]$. Here θ is the angle between the particle's momentum vector and the beam line. This angular variable is called pseudorapidity (η):

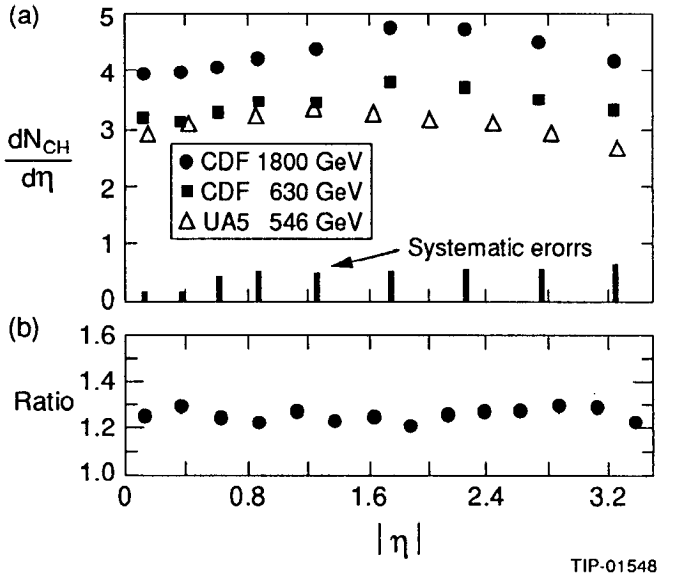

Figure 1 (*a*) The charged particle pseudorapidity distribution $dN_{ch}/d\eta$ as a function of the pseudorapidity η as measured by CDF ($\sqrt{s}$ = 1800, 630 GeV) and by UA5 ($\sqrt{s}$ = 546 GeV) (55). In all cases, the statistical uncertainty is smaller than the plotted point. An estimate of the systematic uncertainty for the CDF data is shown on the lower edge of the plot. (*b*) The ratio of $dN_{ch}/d\eta$ at 1800 GeV to that at 630 GeV.

$$\eta \equiv -\ln[\tan(\theta/2)]. \qquad 4.$$

Because it is independent of mass and therefore requires only an angular measurement, η rather than y is the variable most commonly used at hadron colliders.

Rapidity is a natural phase-space element and the distribution of particles is expected to be roughly flat in this variable. This fact is demonstrated in Figure 1, which shows the charged particle multiplicity $dN_{ch}/d\eta$ as a function of pseudorapidity for several center-of-mass energies. These data were taken using "minimum bias" triggers, triggers sensitive to the complete nondiffractive cross section. At all center-of-mass energies ($\sqrt{s}$), the cross section is nearly independent of η. The value of $dN_{ch}/d\eta$ grows slowly with increasing center-of-mass energy.[2]

[2] Note that the flat rapidity "plateau" must end at some value η_{max}. This value is set by the kinematic limit $\eta_{max} \approx \ln(2E/m)$, where m is the mass of the produced particle, usually a pion.

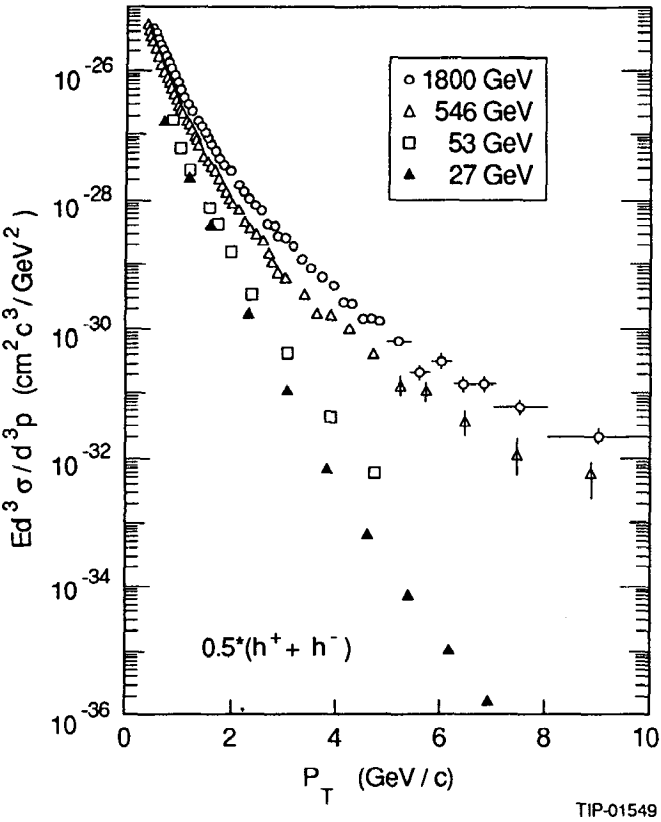

Figure 2 The energy dependence of the single-particle invariant cross section $Ed^3\sigma/d^3p$ as measured by the CDF ($\sqrt{s} = 1800$ GeV) (56), UA1 ($\sqrt{s} = 546$ GeV) (57), British-Scandinavian ($\sqrt{s} = 53$ GeV) (58), and Chicago-Princeton ($\sqrt{s} = 27$ GeV) (59) collaborations.

As can be seen in Figure 2, the single-particle p_t spectrum falls rapidly for minimum bias events. However, as the center-of-mass energy increases, a high p_t tail becomes apparent in the data. The effect is also observed (see Figure 3) in the behavior of the cross section $d\sigma/d\Sigma E_t$, where ΣE_t is the total transverse energy observed in the event:

$$\Sigma E_t \equiv \sum_i E_i \sin\theta_i. \qquad 5.$$

Here E_i is the energy in detector cell i with center at position θ_i and the sum is taken over all detector cells. The nonexponential tail at high

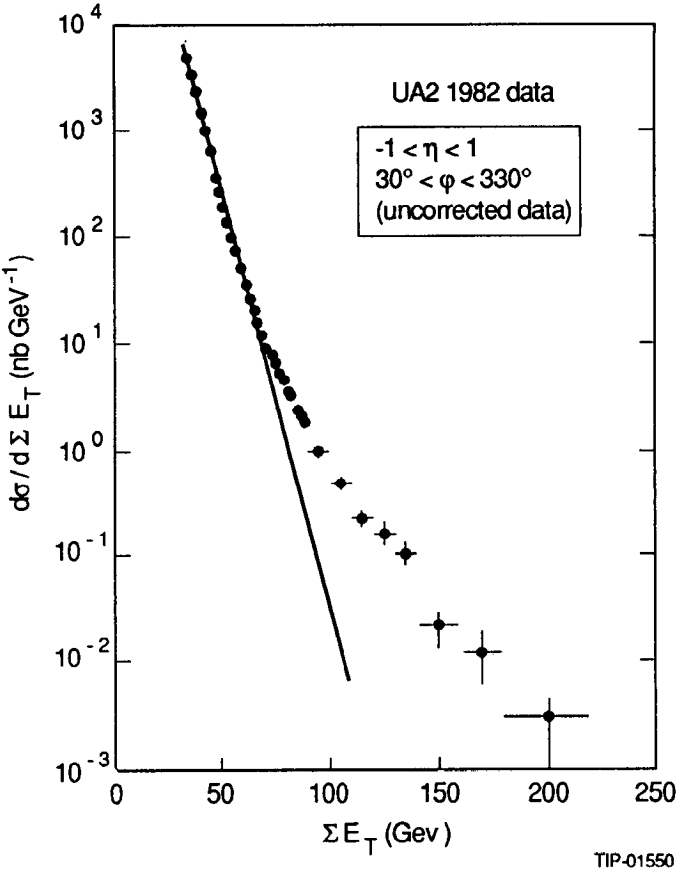

Figure 3 The observed distribution of $d\sigma/d\Sigma E_t$ as a function of ΣE_t as measured by the UA2 experiment. The solid line shows the exponential falloff at low ΣE_t.

transverse energy indicates the presence of a component of the cross section that does not result from the soft physics described above. This is the onset of hard scattering, which is the focus of the remainder of this article. [The high summed E_t tail in the E_t spectrum is a particular example of high p_t phenomena in hadron colliders (for more discussion, see 2).]

1.2 *Large Momentum Transfer Processes*

Because the strong coupling constant α_s becomes small for large momentum transfers, high p_t scattering is well described by perturbative QCD

(for a review of the QCD parton model, see 3). Initial hadrons are treated as a set of quasi-free partons (quarks and gluons) that scatter elastically to produce large p_t partons. The momentum distributions of the initial partons are described by a set of distribution functions $f_i(x, \mu)$ that specify the probability for finding a parton of type i in the proton carrying a fraction of the proton's total momentum that is between x and $x+dx$. Here μ is an arbitrary scale at which the distribution functions are evaluated and should be taken to be of the order of the hard momentum scale Q. The hard scattering process is represented by the following parton model formula:

$$\sigma \approx \sum_{ij} \int dx_1\, dx_2 \hat{\sigma}_{ij} f_i(x_1, \mu) f_j(x_2, \mu). \qquad 6.$$

Here i and j label the types of incoming partons (gluons and the various flavors of quarks and antiquarks) and $f_i(x, \mu)$ is the parton structure function for parton species i. The invariant mass of the parton-parton system ($\sqrt{\hat{s}}$) is related to the hadron-hadron center-of-mass energy ($\sqrt{s}$) by $\hat{s} = x_1 x_2 s$. The parton cross section σ_{ij} can be calculated perturbatively and is expressed as an expansion in $\alpha_s(\mu)$.

At collider energies, the hard scattering cross section is dominated by gluon-gluon scattering. This is true because color factors enhance the gluon cross section relative to quarks and because the gluon structure functions dominate at low x, where the cross section is largest. Independent of Q^2, parton elastic scattering is dominated by t-channel gluon exchange. Thus, the angular distribution in the center of mass is similar to Rutherford scattering:

$$\frac{d\sigma}{d\hat{t}} = \frac{|M|^2}{16\pi\hat{s}^2}, \qquad 7.$$

where $\hat{t}$ and $\hat{s}$ are the normal Mandelstam variables, evaluated in the parton center-of-mass system. High p_t leptons are produced by the weak decays of heavy quarks and electroweak bosons. Their production rates are therefore reduced relative to elastic parton scattering by several orders of magnitude.

The lowest-order QCD calculations provide reasonable descriptions of the inclusive jet and boson cross sections. There is always an ambiguity, however, in the normalization of such calculations because the calculated rate depends on the choice of momentum scale μ used for evaluation of α_s and for the evolution of the quark and gluon distribution functions. This theoretical uncertainty is in general reduced if a next-to-leading-order calculation is done. The contribution of the next-to-leading-order term

has been calculated in several cases: the total cross section for W/Z production and for Drell-Yan scattering ($p\bar{p} \rightarrow e^+e^-$, $\mu^+\mu^-$) (4), the cross section for producing an isolated high transverse momentum photon (5), the total cross section for producing a heavy quark–antiquark pair (6), and the single-jet inclusive cross section (7).

1.3 *Experimental Considerations*

To study hard scattering phenomena, one must measure the properties of quarks and gluons (jets), electroweak bosons (photons, W's, Z's), and neutral, noninteracting particles (neutrinos, supersymmetric particles). Because the total inelastic cross section is so large relative to the hard scattering rate, significant event selection must be accomplished at the trigger level. These considerations place several requirements on any multipurpose detector designed to run at a hadron collider. We review here the general considerations for detector design. Descriptions of the UA1 (8) and UA2 (9) detectors at CERN and the CDF (10 and references therein) and D0 (11) detectors at Fermilab are available in the literature.

The high energies reached in hadron colliders necessitate the use of calorimetric detectors. The high multiplicity environment demands that the detector have good segmentation. The fact that inclusive production is generally flat in rapidity and uniform in ϕ (for a constant E_t cut) means that pseudorapidity and ϕ are natural segmentation variables. A large solid-angle coverage is highly desirable. Because the jet rate dominates all other processes, a high level of rejection against jet events is necessary when studying electrons, muons, and missing-energy signals. For muons and electrons, this means that high quality tracking information is important. In a high rate environment, it is advantagous to have this information available in the trigger. Good calorimeter resolution and the absence of cracks are also necessary to eliminate mismeasured jets as a major source of missing transverse energy.

Typically, collider detectors employ large sampling calorimeters. These detectors have good resolution at high energy and are sensitive to both charged and neutral particles. In most cases many longitudinal samples are summed in depth to form projective "towers" in η-ϕ. Some longitudinal segmentation, however, is essential. Calorimeters are typically divided into "electromagnetic" and "hadronic" sections, often constructed with different materials. The electromagnetic and hadronic segments can also be further subdivided to give additional information about the longitudinal shower development.

Tracking chambers are an essential ingredient of collider detectors, providing a necessary tool for lepton and photon identification. The high overall multiplicity of particles produced in hadronic collisions means that

tracking detectors must have good two-track resolution and must provide high quality extrapolation to calorimeters and muon detectors. While a momentum measurement can aid in background rejection and is necessary for some physics studies (such as the measurement of jet fragmentation functions or the reconstruction of final-state particles such as K^0's, D^0's, B's), it is not essential for a collider detector. Two of the four large $p\bar{p}$ collider detectors (UA2 and D0) have no magnetic field.

The large collider detectors all operate with a number of different triggers. A prescaled minimum bias trigger provides a representative sample of nondiffractive events. Jet triggers select hard scattering events either by requiring a minimum ΣE_t in the calorimeters or requiring a localized cluster of energy above a specified E_t. Electron triggers require an electromagnetic cluster with little hadronic energy and often incorporate a tracking requirement as well. Muon triggers require a set of hits in the muon chamber that point back to the interaction region. Here again, a track requirement can also be imposed.

2. JET PHYSICS

Jet production is the dominant high p_t process at the CERN and Tevatron colliders. The study of such jet events allows high statistics tests of the QCD model of strong interactions. The basic assumption of these measurements is that observed jet cross sections and angular distributions closely follow those of the partonic processes. This assumption relies on our ability to define a prescription for finding jets that is both experimentally straightforward and well matched to the theoretical calculation of interest (for a discussion of jet definition, see 12).

Hadronization is a soft process. Hadrons are therefore produced with limited p_t with respect to the initial parton direction, forming collimated "jets" of particles. In general, hard scattering events appear as two "beam jets" and two or more high p_t scattered jets. The beam jets are remnants of the initial protons and antiprotons after the hard scattering has occurred. The resulting beam jet particle distributions look a great deal like the soft minimum bias events discussed in Section 1.1. The presence of a hard scatter in the event can result in a higher overall multiplicity, but the "underlying event" in hard scattering processes is well described by a flat rapidity distribution of low p_t particles.

In contrast, high p_t jets can be observed as a cluster of energy. Such jets were first unambiguously observed in $p\bar{p}$ collisions by the UA2 experiment in 1982 (13). Using a simple "cluster algorithm" that combined neighboring calorimeter cells, the UA2 group found that for large ΣE_t most of the total energy observed in their calorimeter was deposited in two back-to-

back clusters. Figure 4 shows the fraction of the total observed transverse energy found in the highest (h_1) and two highest (h_2) clusters as a function of the total transverse energy in the event. At high transverse energies, most of the transverse energy E_t is found in the two highest clusters. Figure 5 shows the distribution of the difference in azimuth of the two highest E_t clusters in events with $\Sigma E_t \geq 60$ GeV. The large enhancement at $\phi = 180°$ is what one expects from a hard $2 \rightarrow 2$ scattering process.

The longitudinal momentum distribution of the hadrons in the high p_t jets is governed by phase-space factors. The mathematical formalism developed in Section 1.1 holds in this case as well. Hadrons in jet events have a roughly flat distribution in rapidity that is measured relative to the jet axis. In the laboratory frame, contours of equal particle density form circles in η-ϕ space (14). It is therefore natural to define a jet in terms of the energy flow within a fixed η-ϕ cone. Fixed-cone algorithms have been used by both the UA1 (15) and CDF (16) collaborations and have been incorporated into next-to-leading-order QCD calculations (17).

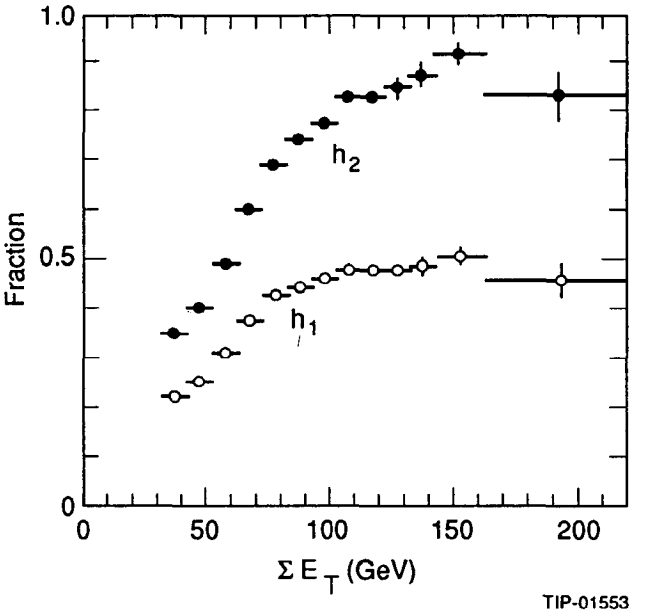

Figure 4 The fraction of the total transverse energy observed in the highest (h_1) and two highest (h_2) clusters as a function of the total transverse energy of the event, as measured by the UA2 experiment.

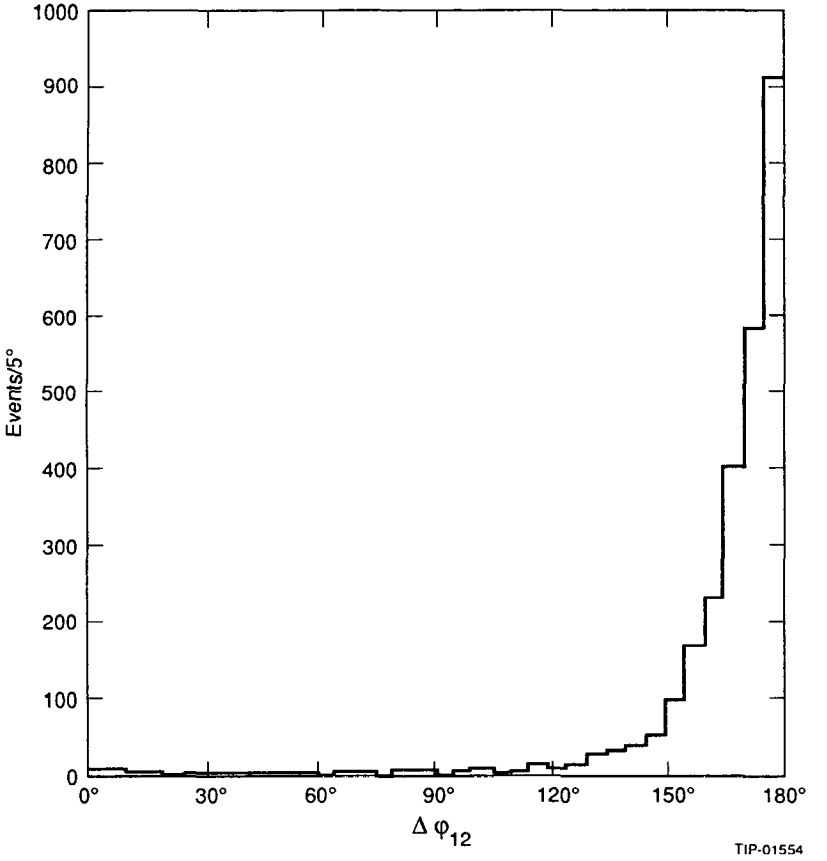

Figure 5 The distribution of the difference in azimuth between the two highest E_t clusters in events with ($\Sigma E_t \geq 60$ GeV), as measured by the UA2 experiment.

2.1 *Single-Jet Cross Section and Compositeness Limits*

At all values of p_t, the jet cross section is dominated by the t-channel exchange of a gluon. Because the matrix elements for all the dominant diagrams are similar, the relative rates of quark-quark, quark-gluon, and gluon-gluon scattering are determined by the parton distribution functions and by color factors. At low $\hat{s}$ gluon scattering dominates, while quark diagrams become important at high $\hat{s}$.

The similarity of the t-channel matrix elements allows us to write the jet cross section using a single effective subprocess (SES) approximation (18):

$$\frac{d\sigma}{dp_t\,dy_1\,dy_2} = F(x_A)F(x_B)\hat{\sigma}_{SES}(AB \to 1,2), \qquad 8.$$

where

$$F(x) = G(x) + \tfrac{4}{9}\Sigma_i[Q_i(X) + \bar{Q}_i(x)], \qquad 9.$$

and the sum is taken over all quark species. UA1 and UA2 have extracted $F(x)$ using inclusive jet data and compared the resulting values to QCD predictions. The results of such a comparison are shown in Figure 6 and demonstrate that the jet cross section at low x cannot be explained by quark-antiquark scattering alone but is in good agreement with the full QCD calculation. This plot provides clear evidence for the non-Abelian nature of QCD and the existence of a three-gluon coupling.

Figure 7 shows the inclusive jet cross section measured by the CDF collaboration. The error bars plotted on the data points include both statistical errors and the portion of the systematic uncertainty that depends on E_t. In addition, the size of the overall normalization uncertainty is indicated in the insert. The curve shown with the data represents the predictions of a next-to-leading-order QCD calculation (17). The normalization uncertainty in this calculation is of order 10%. Both the overall rate and the shape of the data are in good agreement with theory.

The measurement of $d\sigma_{Jet}/dE_t$ can be used to study models of quark compositeness. If quarks are made of more fundamental objects, their strong coupling will be modified. Based on a simple assumption of color-singlet isoscalar exchange between left-handed quarks (19), the Lagrangian for this interaction is

$$\mathcal{L} = \pm \frac{g^2}{2\Lambda_c^2}(\bar{u}_L\gamma^\mu u_L + \bar{d}_L\gamma^\mu d_l)(\bar{u}_L\gamma_\mu u_L + \bar{d}_L\gamma_\mu d_l), \qquad 10.$$

where $g^2/4\pi \equiv 1$. For energies far below Λ_c, this term acts like an effective local four-fermion interaction. The inclusive cross section will contain a term that is independent of $\hat{s}$, and will cause a flattening of the cross section as a function of E_t, that is, an excess of events in the high E_t region.

Figure 8 shows a preliminary measurement of $d\sigma/dE_t$ from the CDF experiment, along with the predictions of QCD and predictions for the composite model described above with a value of $\Lambda_c = 950$ GeV. Although a compositeness limit has not yet been set using this data, it is clear that values of Λ_c below about a TeV are excluded (20). Recent results from the UA2 collaboration give a lower limit for Λ_c of 825 GeV at a 95% confidence level (21).

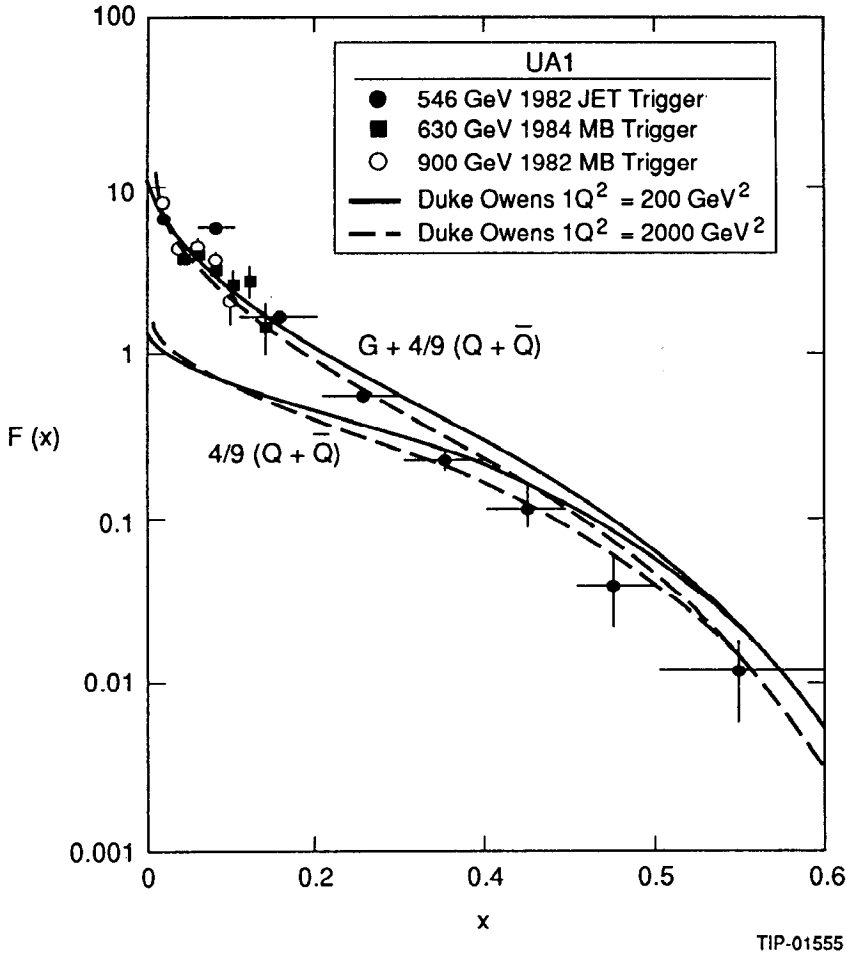

Figure 6 The effective structure function as measured by the UA1 experiment. The curves show the QCD predictions at two values of scale, with and without the gluon contribution.

2.2 *Two-Jet Angular Distribution*

The majority of hard scattering events contain two back-to-back jets. This dijet system can be described in terms of six independent variables, three boost variables that transform to the hard scattering center of mass (β_x, β_y, and β_z) plus three center-of-mass variables ($\hat{s}$, the invariant mass of the hard scattering system, ϕ the azimuthal position of one of the jets, and

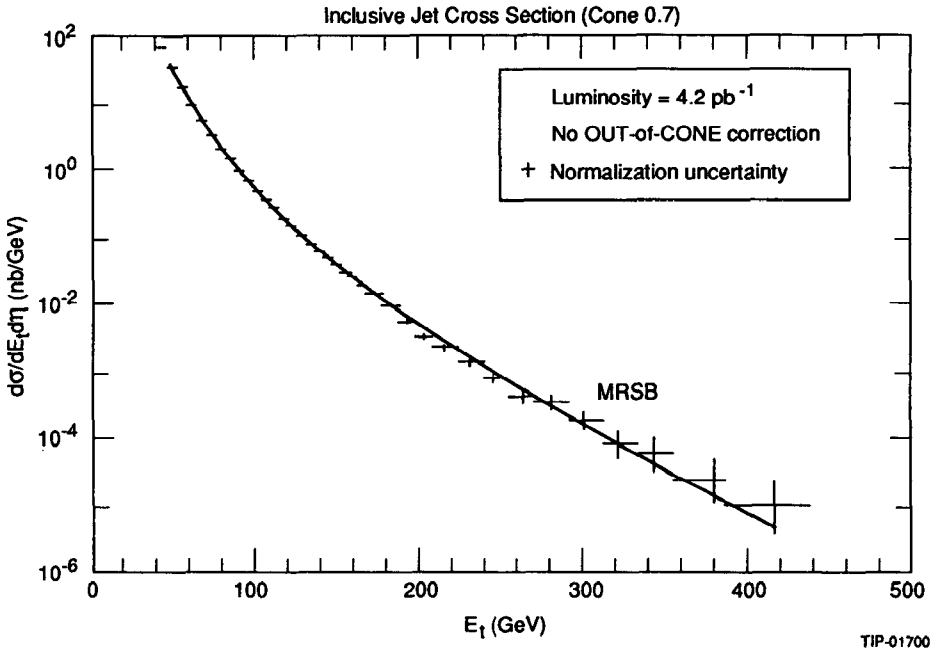

Figure 7 The single-jet inclusive cross section as measured by CDF. The data are compared to a calculation of order(α_s^3).

cos θ^*, the scattering angle of one of the jets with respect to the beam line). The distributions in two of these six variables, β_z and $\hat{s}$, are determined primarily by the parton distribution functions. The azimuth, ϕ, shows no dynamical structure for unpolarized beams.

The transverse boosts β_x and β_y result from higher-order QCD processes. These boosts are often described by the phrase "intrinsic k_t" and are caused by the emission of additional gluons during the hard scattering process. In all collider experiments, the observed dijet k_t results from two sources, the intrinsic k_t caused by gluon emission and experimental effects such as finite energy resolution. The UA2 group has developed a technique for separating these two effects. The mean value of k_t is about 5 GeV (22).

Because there is a t-channel pole in the cross section, the distribution in cos θ^* takes on a Rutherford-like shape:

$$\frac{d\sigma}{d\cos\theta^*} \approx \alpha_s^2(\mu)\hat{s}\frac{1}{1-\cos^2\theta^*}. \qquad 11.$$

This form represents the expected angular distribution for a fixed cutoff

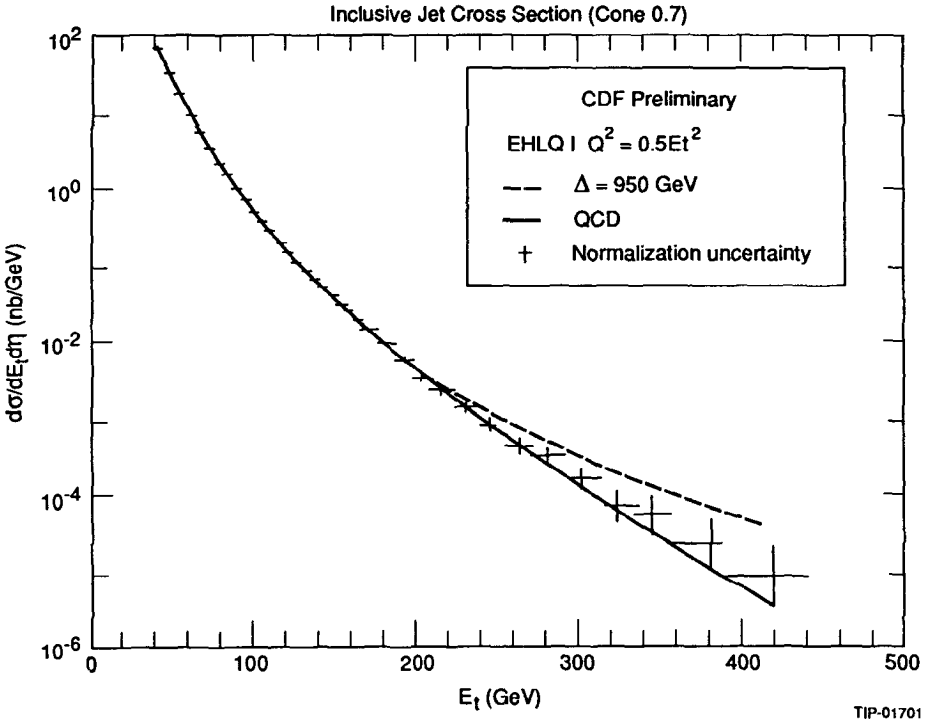

Figure 8 The inclusive cross section as measured by CDF. The predictions of QCD (EHLQ, Set I structure functions with $Q^2 = 0.5E_t^2$) and QCD modified by a compositeness term with $\Delta = \Lambda_c = 950$ MeV.

in parton invariant mass and for a fixed range in the boost parameter β_z. It is common to plot the dijet angular distribution in terms of the variable χ:

$$\chi \equiv \hat{u}/\hat{t} = \frac{1+\cos\theta^*}{1-\cos\theta^*} \approx e^{|\eta_1-\eta_2|}. \qquad 12.$$

The distribution in χ is approximately constant for $\chi > 2$:

$$\frac{d\sigma}{d\chi} \approx \frac{\pi\alpha_s^2(Q^2)}{\hat{s}} \frac{(\chi^{-2}+\chi^{-1}+1+\chi+\chi^2)}{(1+\chi)^2}. \qquad 13.$$

Figure 9 shows the χ distribution as measured by UA1, along with QCD predictions (23). The figure shows that the parton model description pro-

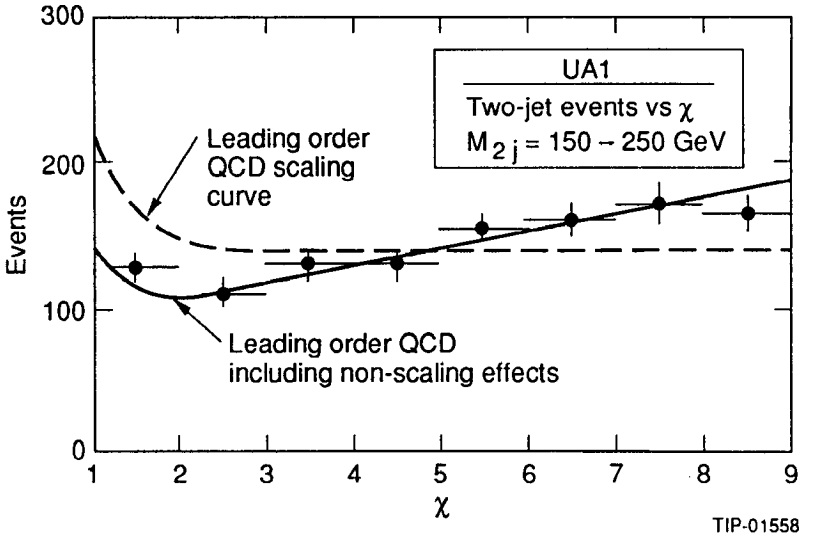

Figure 9 The distribution of χ for two-jet events as measured by the UA1 collaboration. The curve shows the predictions of a lowest-order two-parton scattering QCD calculation, with and without contributions due to QCD scaling violations.

vides a good description of the data if one includes the effect of scaling violations in the calculation.

2.3 *Three-Jet Angular Distributions*

The production of three-jet events is common at collider energies. These events result from the production of a hard gluon via initial- or final-state bremsstrahlung (24). The three-jet fraction is a strong function of the minimum p_t cut on the third jet; typically $\sim$20% of all jet events show a third jet.

The scattering of three massless partons can be described by nine independent variables. As in the two-jet case, there are three boost variables (β_x, β_y, and β_z). The distribution of energy in the center-of-mass system is described by three internal variables: $\hat{s}$, the invariant mass of the three-jet system, and x_3 and x_4, the energy fractions of the two leading jets.[3] In addition, the orientation of the three-jet system can be described by three Euler-like angles: θ^*, the angle between the leading jet and the beam line,

[3] These variables are scaled to the subprocess center-of-mass energy such that $x_3+x_4+x_5=2$.

ϕ^*, the azimuthal position of the leading jet, and ψ^*, the angle of rotation about the leading jet axis (ψ^* is the angle between the plane formed by the leading jet and the beam line and the plane formed by the two other jets).

The cos θ^* distribution for three-jet events is nearly identical in shape to that for the two-jet system (25). As in the two-jet case, the dominant three-jet diagrams involve the t-channel exchange of a gluon propagator. The angular distribution in ϕ is flat since the initial partons are unpolarized, but the ψ^* distribution peaks at 0° and 180°. This structure is the result of singularities in the cross section for gluon radiation along the beam line. The regions of ψ^* near 0° and 180° are experimentally difficult to measure because the p_t of the softest jet decreases rapidly as the three-jet system is rotated into a configuration where the three jets are planar with the beam line.

Figures 10 and 11 show the distributions of the variables x_3 and x_4 as measured by the CDF experiment (26). The solid lines show the shapes these distributions would have in a phase-space model, while the diamonds

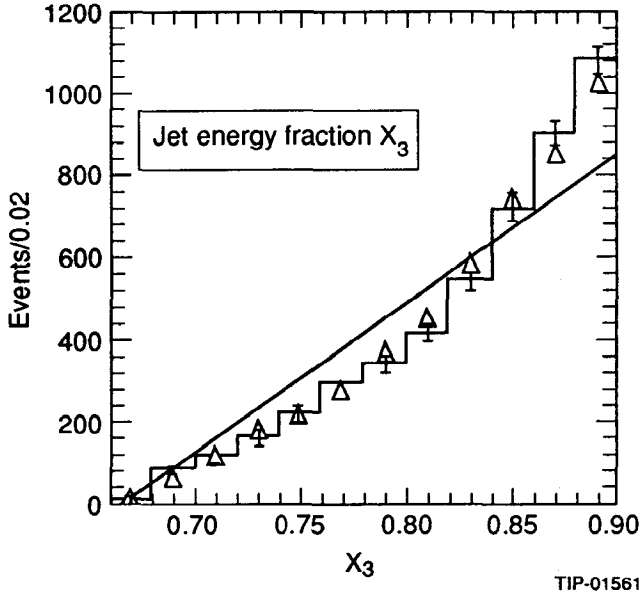

Figure 10 The distributions of the variable x_3 as measured by CDF (histogram). The solid line is the prediction of a phase-space model while the diamonds show the QCD predictions.

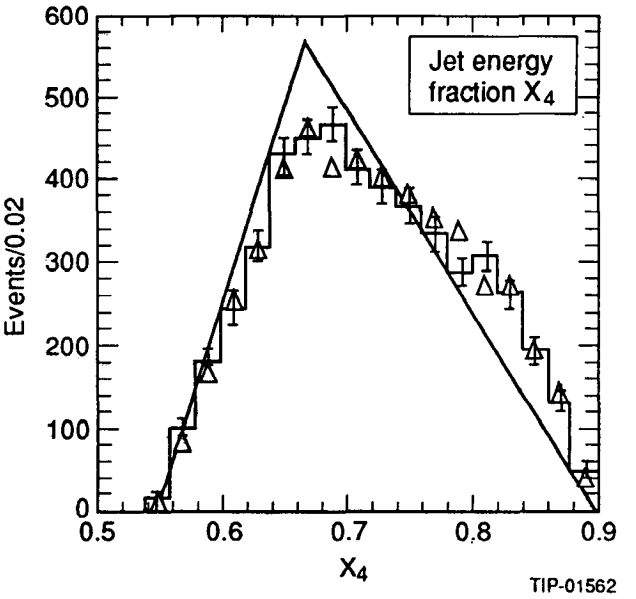

Figure 11 The distributions of the variable x_4 as measured by CDF (histogram). The solid line is the prediction of a phase-space model while the diamonds show the QCD predictions.

show the predictions of a QCD calculation. For both variables, QCD provides a good description of the data. Significant deviations from the phase-space model are seen. These plots provide evidence that three-jet events result from a bremsstrahl process.

In summary, the dynamics of jet production is well described by perturbative QCD. Quantitative agreement between theory and experiment exists over a wide kinematic range, not only for the inclusive cross section but for angular and energy variables as well. This agreement is essential to our understanding of collider physics. Since the hard scattering cross section is dominated by QCD processes, a thorough understanding of QCD phenomena is important for interpreting all collider results.

3. LEPTON IDENTIFICATION

Leptonic decays provide an important tag of electroweak processes at hadron colliders. The presence of leptons can be used to select relatively

pure samples of W and Z bosons and heavy quarks. At collider energies, however, leptons from the decay of bottom quarks are produced with low to moderate p_t; even leptons from W's and Z's have transverse momenta well below those for typical QCD jets. Jet production presents a large background to the study of low p_t leptons and must be rejected at the trigger level.

Both electron and muon identification can be enhanced with isolation cuts. Such cuts remove events with significant additional energy deposition near the lepton. Isolation criteria are sensitive to the production process and the mass of the decaying particle. Standard Model processes that tend to produce isolated leptons include Drell-Yan and weak Drell-Yan processes, and heavy quark decay for very massive top quarks. Processes that produce nonisolated leptons include b and c quark decays.

3.1 *Electron Identification*

The CDF experiment provides an example of electron identification in a magnetic detector (27). The CDF central electron trigger requires an electromagnetic energy deposit of $E_t > 12$ GeV within a "trigger tower" ($\delta\eta = 0.2, \delta\phi = 15°$) in association with a track of $p_t > 6$ GeV/c. The ratio of hadronic to electromagnetic energy in the calorimeter is required to be less than 0.125 in the trigger. This sample contains significant background from π^0-π^+ overlap, early-showering charged pions, and photon conversions and Dalitz pairs. Such backgrounds are rejected in the offline analysis in the following manner:

1. A requirement is made that the measured track momentum (p) and calorimeter energy deposit (E) be consistent (a typical cut is $E/p < 1.5$).

2. The requirement that the leakage into the hadronic section of the calorimeter be small is tightened. The ratio of hadronic to electromagnetic energy must be less than 0.05.

3. Gas proportional chambers with cathode strip readout ("strip chambers") imbedded in the calorimeter near shower maximum provide an accurate measurement of the shower position. This position can be compared to the extrapolated track position measured by the Central Tracking Chamber.

4. Events containing a single charged track and multiple π^0's are rejected by requiring the transverse spread of the electromagnetic cluster to be consistent with that expected for an electron. The lateral shape is measured in the calorimeter by studying the fraction of the energy deposited in the towers surrounding the central one hit by the electron candidate. A measurement of this shape is also made in the strip chambers, where a χ^2 test to the electron hypothesis is performed in both the wire and the strip projections.

5. Conversion electrons and Dalitz pairs are identified in the tracking chambers. The CDF algorithm is estimated to be $\sim 80\%$ efficient at finding conversions.

The UA2 detector does not have a magnetic field and hence cannot use E/p as a tool for selecting electrons. Nevertheless, the experiment has excellent electron identification (28). As in the magnetic detectors, the major methods for rejecting background are (*a*) requiring the electron candidate have both longitudinal and transverse shower development consistent with that expected for a single electromagnetic shower, and (*b*) requiring a good match between the position of the electromagnetic cluster and the extrapolated track position at the face of the calorimeter. In the UA2 detector this track position is measured using a preshower converter consisting of 1.5 radiation lengths of tungsten followed by a proportional chamber to provide a good position measurement. In an effort to improve the background rejection for lower energy and less isolated electrons from top and bottom quark decay, a major upgrade of UA2 added the following features:

1. A cylindrical drift chamber (Jet Vertex Detector). Its purpose was to measure tracks close to the beam interaction point.
2. A highly segmented silicon hodoscope. The hodoscope rejected conversion pairs by measuring dE/dx losses.
3. A scintillating fiber detector (SFD). It provided a measurement of the track position immediately in front of the central calorimeter and served as a preshower counter.
4. A transition radiation detector (TRD). This provided an independent method for separating electrons and pions.

The additional background rejection from the combination of added detector components was about a factor of 20.

3.2 *Muon Identification*

The principles of muon identification are presented here, using the UA1 experiment as an example (29). Muons in the UA1 detector are measured with two sets of chambers separated by 60 cm. Each set contains planes of drift chambers and limited steamer tubes. The coverage is $\approx 70\%$ of the full solid angle and the detector is placed behind approximately nine interaction lengths of iron.

The UA1 muon trigger requires a muon track "stub" consisting of at least three out of four possible hits in the chamber. The track must point back to the interaction region within a cone of ± 150 mrad. The thickness of the absorber and the pointing requirement translate to an effective minimum p_t cut of about 2 GeV on the muon trigger.

About 40% of the events written to tape by the UA1 collaboration are triggered by the muon system (29). These data are analyzed in the following manner. A filter is applied to remove cosmic rays, events with shower leakage through the calorimeter cracks and central detector tracks with obvious kinks. Muon candidates are selected by requiring a good match between the muon stub and the track measured in the central drift chamber. Single-muon events are selected by requiring a track candidate with $p_t > 6$ GeV and $|\eta| < 1.5$. A dimuon sample is selected by requiring $p_t > 3$ GeV and $|\eta| < 2.0$ for each muon (with at least one muon satisfying $|\eta| < 1.3$), and the mass of the muon pair to exceed 6 GeV.

The residual background in these samples is dominated by decays of pions and kaons and the background from misassociation of tracks in the central detector and the muon detector (≈ 0.07 per muon). Other backgrounds include noninteracting hadrons, shower leakage, particles penetrating cracks, and residual cosmic rays (total ≈ 0.025 per muon). The π and K decay background is reliably estimated by folding the measured single-hadron p_t spectrum with the probability that a hadron of a given p_t will decay to a muon with p_t^μ. That is,

$$\frac{d\sigma^{\text{background}}}{dp_t^\mu} = \int \frac{d\sigma}{dp_t^{\text{hadrons}}} \text{Prob}(p_t^{\text{hadron}} \to p_t^\mu)\, dp_t^{\text{hadron}}, \qquad 14.$$

where the probability $\text{Prob}(p_t^{\text{hadron}} \to p_t^\mu)$ is estimated using Monte Carlo techniques. For isolated muons, a requirement that the energy deposited in the calorimeter be consistent with minimum ionizing deposition can also be applied.

The size of the background in the muon sample is quite dependent on the physics process being studied. The background decreases rapidly with p_t. In addition, since most hadrons are produced within jets, an isolation cut will significantly improve the signal-to-noise ratio.

3.3 *Neutrino Identification*

Electroweak decays often involve the production of neutrinos. Since these particles cannot be detected directly, their presence must be inferred from the presence of a large momentum imbalance in the event. Because all collider detectors have holes in the forward and backward region to allow the beam to enter and exit the apparatus, no detector is capable of measuring the energy flow in the beam direction. Instead, the technique for finding noninteracting neutral particles involves the search for large missing transverse momentum.

Calorimetric detectors have the advantage that they are sensitive both

to charged and neutral particles. They are therefore the most suitable for missing-momentum measurements. Because a calorimeter measures energy rather than momentum, the term "missing E_t" ($\not{E}_t$) is usually used to describe the magnitude of the missing transverse momentum. We define the missing transverse energy by the relation

$$\not{E}_t \equiv -\sum_i \mathbf{E}_t = -\sum_i E_t \hat{\mathbf{n}}_i, \qquad 15.$$

where the sum is over towers in the calorimeter and where $\hat{\mathbf{n}}_i$ is the outward-pointing normal to the tower center.

An $\not{E}_t$ analysis is sensitive to all types of detector imperfections. Backgrounds for $\not{E}_t$ analyses include mismeasurement of jet events due to finite detector resolution, loss of energy in cracks, and loss of jets in the beam direction. For both the UA1 and CDF experiments, and for the upgraded UA2 detector, mismeasured jets are the primary source of $\not{E}_t$.

For sampling calorimeters, the resolution in general scales with the square root of the incident energy. If the missing E_t resolution is dominated by calorimeter effects, then the fractional E_t resolution should scale as $1/\sqrt{\Sigma E_t}$. The UA1 group and later the CDF group have studied the E_t resolution and have found that this form holds. They therefore define the "missing E_t significance" to be

$$S \equiv \frac{\not{E}_t}{\sqrt{\Sigma E_t}}. \qquad 16.$$

4. ELECTROWEAK PHYSICS

The study of electroweak gauge bosons is a major element of collider physics. The $W^{\pm}$ and Z^0 were first discovered in hadron collisions. Such collisions remain as yet the only way of producing charged vector bosons. The large QCD background inhibits the study of hadronic decays of the W and Z. Although a combined W/Z signal has been observed by UA2 in the dijet invariant mass distribution (31), most studies at hadron colliders have been limited to leptonic decays.

Collider studies of the W and Z have two major thrusts. First, measurements of the boson production properties provide tests of perturbative QCD. Second, measurements of the boson masses and decay distributions provide information on the electroweak structure of nature. In particular, precision measurements of the W mass, in conjunction with results from LEP and from deep inelastic neutrino scattering, provide an important check of electroweak radiative corrections (e.g. 32).

4.1 *W Boson Production and Decay*

The lowest-order process for producing W or Z bosons in a $p\bar{p}$ collider is quark-antiquark annihilation (33). This process produces no transverse momentum, and hence for leptonic decays the two leptons must balance p_t. Higher-order calculations of the W production cross section have been completed, with the following results (34): The total cross section changes by an overall factor $K \approx 1 + 8\pi/9\alpha_s(M_W^2)$. In addition, the W does not have zero p_t. A correct calculation of the transverse momentum spectrum for W bosons requires a nonperturbative treatment of multiple soft gluon emission, which is handled via resummation techniques (35). The mean transverse momentum of the W is of order 10 GeV. The measured W production cross section (multiplied by the leptonic branching ratio, B) at SPS and Tevatron energies, $\sigma B = 2.6 \pm 0.6 \pm 0.5$ nb at the Tevatron, is in good agreement with these predictions (36). Figure 12*a* shows the transverse momentum distribution of W candidates, as measured by the UA2 collaboration (37). The curves show QCD predictions (including soft gluon resummation) as a function of the value of Λ_{QCD} used to evaluate α_s. Figure 12*b* shows the predictions at high p_t in more detail. The agreement with theory is excellent.

The angular distribution of W decays is determined by helicity conservation and the spin-1 nature of the W. For $W^+ \to e^+ \nu$, the e^+ is preferentially produced along the $\bar{p}$ direction, and the angular distribution in the center-of-mass system is

$$\frac{d\sigma}{d\cos\theta} \approx \frac{\hat{s}(1+\cos\theta)^2}{(\hat{s}-M_W^2)^2+(\Gamma_W M_W)^2}, \qquad 17.$$

where M_W and Γ_W are the mass and decay width of the W, respectively. A transformation of variables allows us to find the electron p_t distribution (here we use the lowest-order calculation, where the W transverse momentum is constrained to be zero). In the center-of-mass frame, the e and ν are back to back and balance p_t. Thus $p_t^2 = \frac{1}{4}\hat{s}\sin\theta^2$. Evaluating the Jacobian

$$\frac{d\cos\theta}{dp_t^2} = -\frac{2}{\hat{s}}\left(1-4\frac{p_t^2}{\hat{s}}\right)^{-1/2} = -\frac{2}{\hat{s}\cos\theta} \qquad 18.$$

gives the result

$$\frac{d\sigma}{dp_t} \approx \frac{1+\cos^2\theta}{\cos\theta} \sim \frac{1-2p_t^2/\hat{s}}{(1-4p_t^4/\hat{s})^{1/2}}. \qquad 19.$$

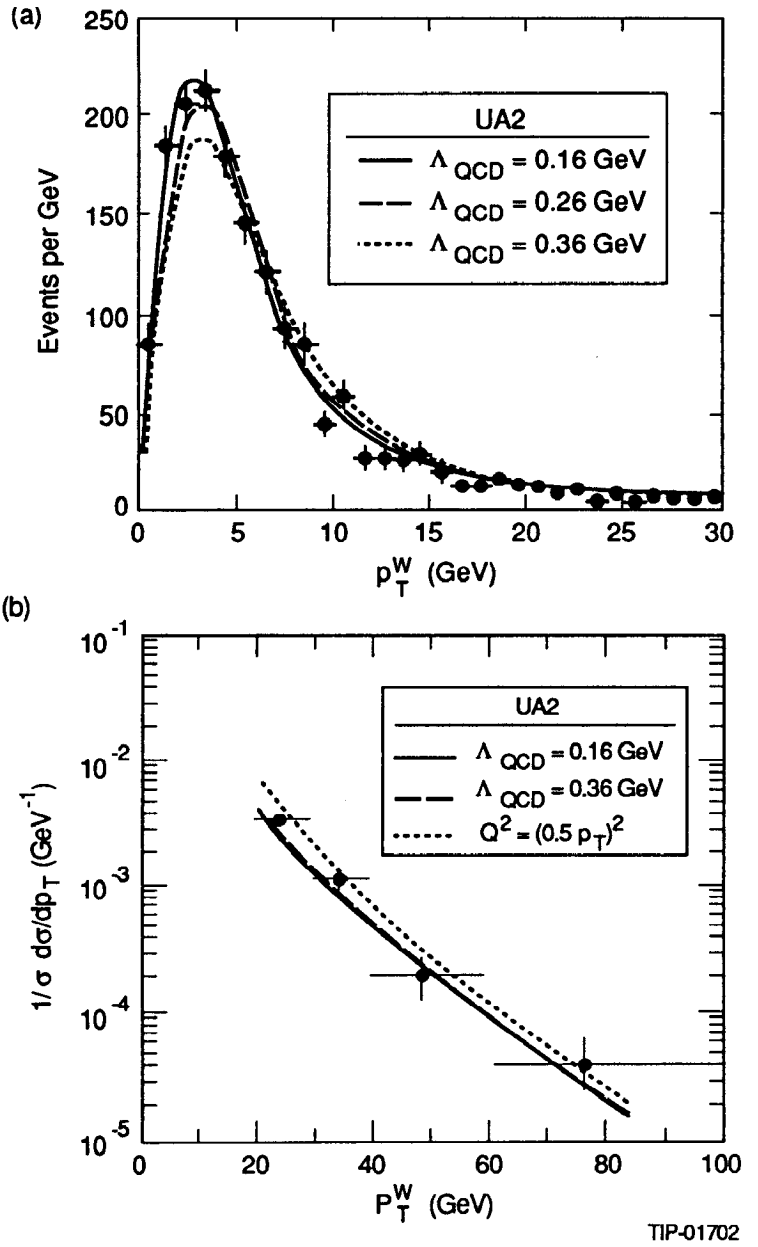

Figure 12 The W boson p_t distribution observed by UA2: (*a*) for $p_t < 30$ GeV, the curves show three different values of Λ_{QCD}; (*b*) the differential cross section for high p_t W production along with the QCD predictions for various Λ_{QCD} and scales Q^2.

The cross section diverges for $\theta = \pi/2$ (and $p_t = \sqrt{\hat{s}}/2$). This divergence is called the Jacobian peak. When the above expression is integrated over all values of $\hat{s}$, the presence of the Breit-Wigner removes the singularity but leaves a sharp peak at $p_t = \sqrt{\hat{s}}/2$. Thus, the lepton p_t spectrum is a good estimator of the W mass.

The nonzero transverse momentum spectrum of the W boson smears the electron and neutrino Jacobian peaks. In order to determine the mass of the W most accurately, one should find a variable that is less sensitive to the smearing. The natural choice is the transverse mass. If a W is produced with transverse momentum, its decay products must both be boosted. The e-ν transverse mass is defined to be

$$m_T^2 = (|p_{t_e}| + |p_{t_\nu}|)^2 - (\vec{p}_{t_e} + \vec{p}_{t_\nu})^2 \qquad 20.$$

and depends on the p_t of the W only to order $(p_t/M_W)^2$. Figure 13 shows the W transverse mass distribution as measured by CDF (38). When fitting for the W mass, CDF has chosen to select a clean W sample by requiring that the event have no additional clusters (in addition to the lepton candidate) with $E_t > 7$ GeV. The curves are a fit to the data using a model that includes the predicted QCD cross section and angular distribution and the effect of finite detector resolution. The value of the mass obtained in this way is $M_W = 79.97 \pm 0.35 \pm 0.24$ GeV for decays to electrons, and $79.90 \pm 0.53 \pm 0.32$ GeV for muons, where the first error is statistical and the second is systematic. Results are in good agreement with and have similar errors to those obtained by the UA2 group: $M_W = 80.49 \pm 0.43 \pm 0.24$ GeV (39).

4.2 *Z Boson Production*

The production of a Z and its subsequent decay into two leptons provides an extremely clean signal. Figure 14 shows the dilepton mass distribution as measured by CDF for (*a*) muons and (*b*) electrons (40). The mass value derived from a combined fit for both decay modes is $M_Z = 90.9 \pm 0.3 \pm 0.2$ GeV. This result should be compared to the LEP result of $M_Z = 91.16 \pm 0.03$ GeV (41). Although the error is larger for CDF than for the LEP experiments, the measurement is of remarkable precision. Z production cross secions and p_t spectra both agree with QCD expectations (42).

The measurement of the ratio of the W and Z production cross sections with subsequent decays into electron(s),

$$R = \frac{\sigma(W \to e\nu)}{\sigma(Z \to ee)}, \qquad 21.$$

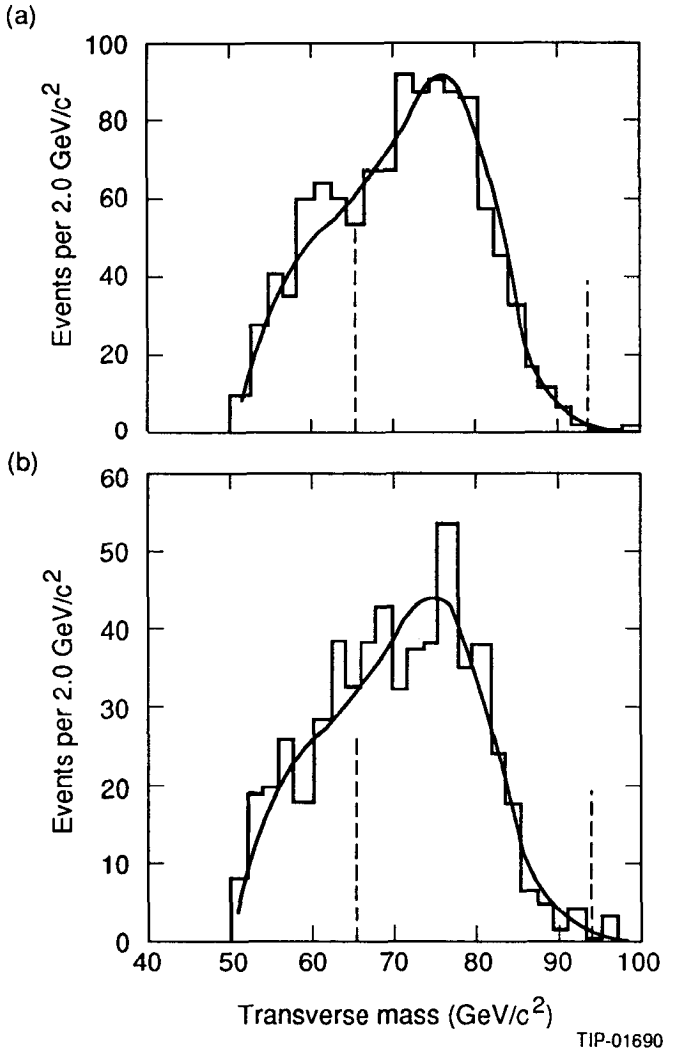

Figure 13 The transverse mass distribution measured by CDF for (*a*) $W \rightarrow e\nu$ and (*b*) $W \rightarrow \mu\nu$ candidates, along with the best mass fit to the data. The range of transverse mass used in the fit is indicated by the dashes.

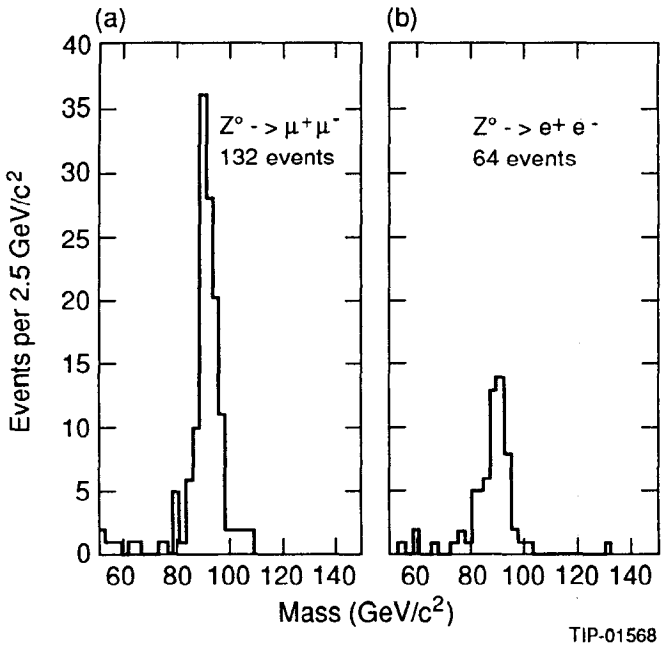

Figure 14 Number of events vs invariant mass distributions by CDF for (*a*) $Z \rightarrow \mu^+\mu^-$ candidates and (*b*) $Z \rightarrow e^+e^-$ candidates as measured with the track detector.

together with the LEP measurement of the total decay with the Z (Γ_Z), allows the total decay width of the W (Γ_W) to be calculated with greater precision than that obtained by direct measurement. The CDF measurement of $R = 10.2 \pm 0.8 \pm 0.4$ yields a result $\Gamma_W = 2.19 \pm 0.20$ GeV (43). The measurement of R provides a method for placing limits on the top quark mass that are independent of the top decay mode. The CDF R measurement excludes M_t below 41 GeV (35 GeV) at the 90% (95%) confidence level. With the existing statistical and systematic uncertainties, this limit is less stringent than those obtained at LEP (44).

5. HEAVY FLAVOR PRODUCTION

5.1 *Bottom Production*

The production of b quarks can be studied in hadron colliders by tagging their semileptonic decays. At CERN and Tevatron energies, b quarks are the most copious source of prompt leptons in the range $5 \leq p_t \leq 20$ GeV. At higher transverse momenta, the dominant mechanism for producing leptons is the decay of weak vector bosons. Figure 15 shows the inclusive

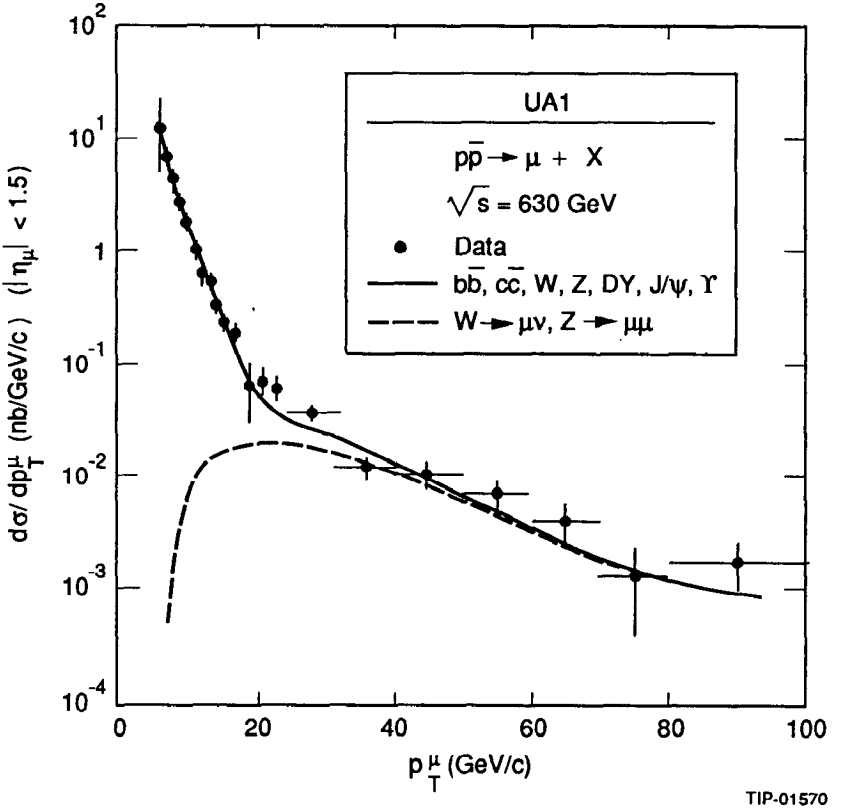

Figure 15 Inclusive muon transverse momentum spectrum for muons measured by UA1. The data are compared with Monte Carlo predictions including the production of $b\bar{b}$, $c\bar{c}$, W, Z, Drell-Yan, J/ψ, and Υ. The data have been corrected for background and acceptance, but not for momentum resolution errors.

muon spectrum as measured by the UA1 collaboration (45). This spectrum is well described by Standard Model lepton sources. The combined contribution of $W \rightarrow \mu\nu$ and $Z \rightarrow \mu\mu$ decays is indicated by the dashed line. The remainder of the spectrum is dominated by b quark decays.

UA1 has studied the relative contributions of b quark, c quark, and π and K decays to the muon spectrum both in single-muon and dimuon events. Figure 16 shows several results from this study for event samples containing like-sign and unlike-sign muon pairs. Figures 16*a* and *b* show the distribution of muons as a function of the muon transverse momentum measured with respect to the direction of the nearest jet (p_t^{rel}).

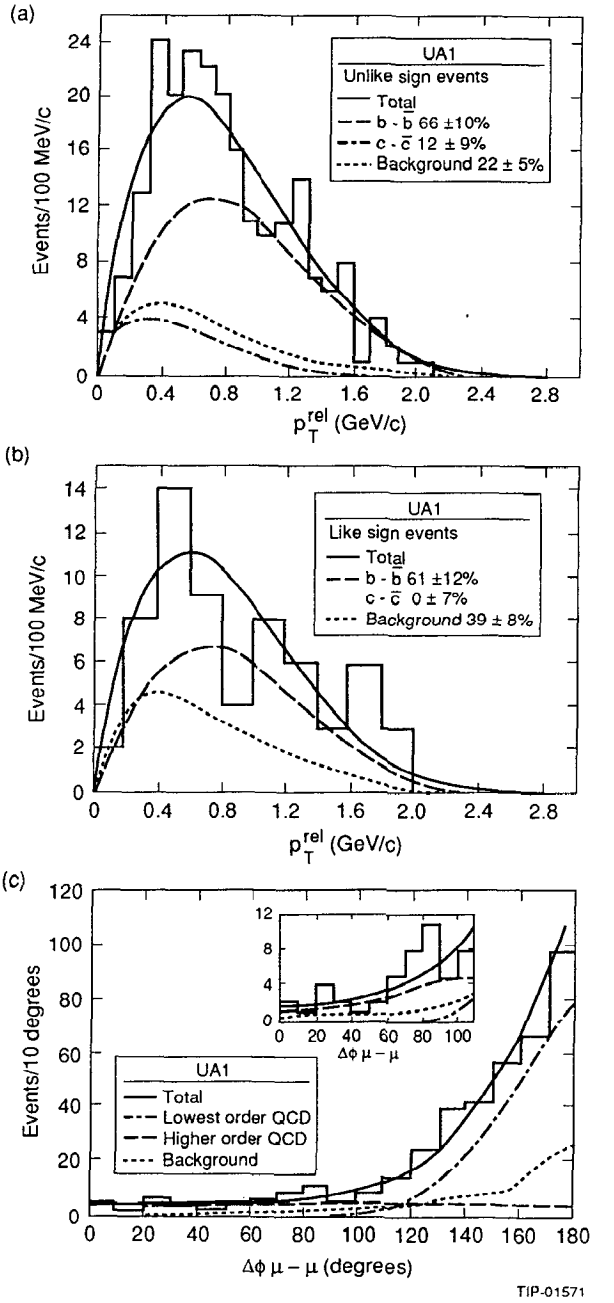

Figure 16 The distribution of p_t relative to the jet axis for muons in dimuon events, as measured by UA1.

Since b quarks are massive, they tend to produce leptons with higher p_t^{rel} than do c quarks. Heavier quarks, such as top, produce even more isolated leptons. The subject of b quark production is an area of active work in CDF (46). Preliminary results on exclusive states such as $B^+ \rightarrow J/\psi K^+$ show that b physics studies at hadron machines hold future promise in their own right. The earlier UA1 work was largely aimed at setting top quark mass limits, by studying lepton isolation distributions. More recent direct searches by CDF and UA2 based on larger data samples have since set more interesting limits.

5.2 *Top Searches*

The Standard Model requires the existence of a top quark, t, the SU(2) partner to the bottom quark. The nonobservation of the t at LEP and SLC places a model-independent lower limit on m_t of 45.8 GeV (44). Upper limits on the top quark mass arise from consideration of the consistency of radiative corrections and the various measurements of the Standard Model parameters. Kennedy & Langacker find $m_t < 190$ GeV at 95% confidence level for Higgs masses in the range $M_Z \leq M_H \leq 1$ TeV (47).

Next-to-leading-order calculations of the top quark production cross section in hadron colliders have been performed (48). For the CERN experiments, the $W \rightarrow t\bar{b}$ process dominates for 40 GeV $< m_t < M_W$, while at the Tevatron the dominant process is $p\bar{p} \rightarrow t\bar{t}$ throughout the mass range. In order to set limits on top quark production, semileptonic decay modes are used to reduce background from Standard Model processes. The transverse momentum of the leptons from such decays can be rather low, depending on the top quark mass: These leptons must be separated from b and c quark semileptonic decays. In addition, since the derived limit depends on the assumed $t \rightarrow$ lepton decay rate, the limit applies only to a Standard Model top quark. In models containing more than one Higgs doublet, the decay of the t to a charged Higgs boson will reduce the sensitivity of the leptonic search.

To search directly for leptons originating from top quark decay, the CDF collaboration uses both electron and muon decay modes (49). For events in which two heavy quarks decay semileptonically, the signature is two oppositely charged leptons among the final-state decay products. The cleanest combination from the point of view of other Standard Model backgrounds is the presence of one e and one μ in the event. This mode has no Drell-Yell background or direct Z decay contamination and, in spite of the small branching fraction, can be used to set interesting limits. Events are selected that contain oppositely charged electron-muon pairs above a p_t threshold. Figure 17 shows the predicted number of events above thresholds between 5 and 40 GeV for the signal with various top

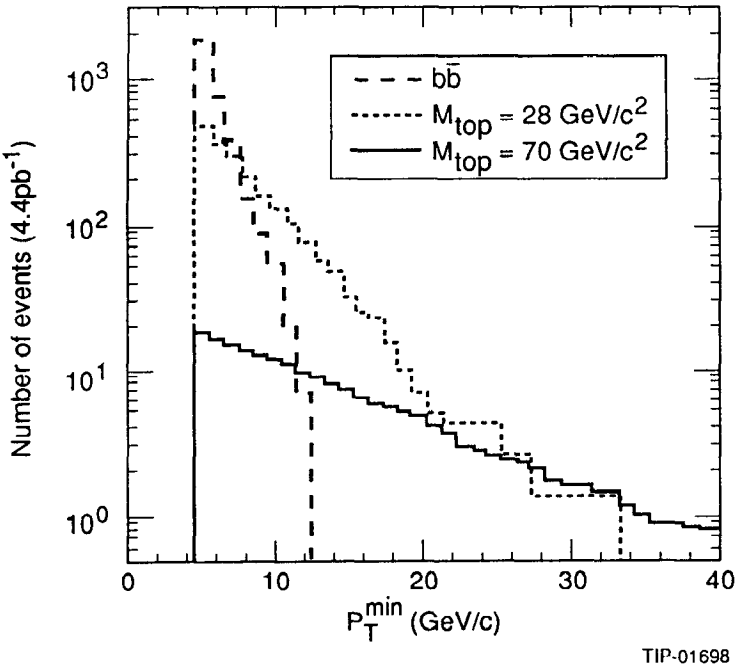

Figure 17 The predicted number of $\mu^{\pm}e^{\mp}$ events with both the E_t of the electron and the P_t of the muon greater than P_t^{min}. The histograms are for $b\bar{b}$ and $t\bar{t}$ production as indicated.

masses and the residual $b\bar{b}$ background. In addition to the electron and muon identification cuts discussed previously, "isolation" cuts are made that eliminate candidate leptons with any extra E_t (>5 GeV) in a cone (radius $R = 0.4$ in η-ϕ) about the lepton direction. The isolation cut serves to reduce the $b\bar{b}$ background so that by setting the lepton p_t threshold to 15 GeV, the $b\bar{b}$ background is largely eliminated while retaining good efficiency for the top signal. One event is observed by CDF with both leptons above 15 GeV p_t, resulting in a lower limit on the top mass of 72 GeV (95% confidence level) (Figure 18) (49). This limit has since been raised to 89 GeV by combining the above data with a sample of dielectron candidates and by lowering the minimum p_t cut on the muon (50).

Another event topology with higher branching fraction, but significant background from W+jets production, is an event with one semileptonic decay mode, and the second top quark decays to jets. Both UA2 (51) and CDF (52) have used this channel to set limits. The transverse mass variable was used to search for an excess of events below the W Jacobian peak. The event selection required an electron, missing $E_t > 20$ GeV, and two

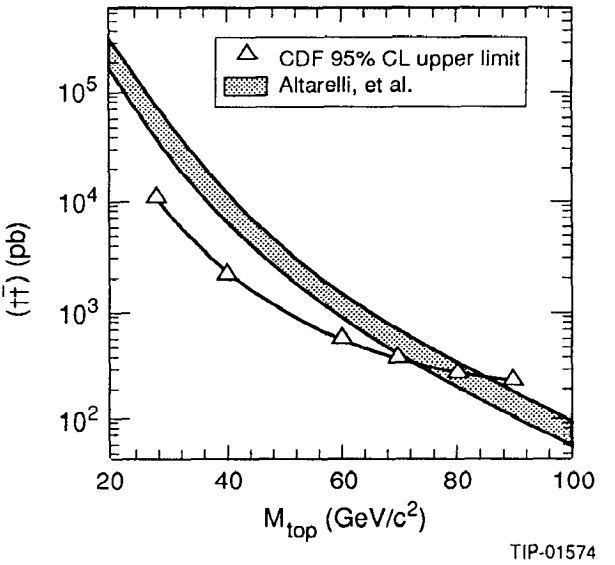

Figure 18 CDF results on the upper limit (95% confidence level) for the $t\bar{t}$ production cross section as a function of the top quark mass. The shaded band shows the result of a theoretical calculation of the $t\bar{t}$ production cross section.

or more jets with $E_t > 10$ GeV (Figure 19). The 95% confidence level lower limits obtained by this method are 77 GeV for CDF (52) and 69 GeV for UA2 (51), see Figure 20. The method based on the transverse mass distribution becomes less effective as the top quark mass limit approaches the W mass, since the changes in shape of the distribution become smaller, and the normalization of the distribution, as calculated in QCD, is somewhat uncertain.

For top quark masses above the W mass, the decay of the top leads to the production of a real W. The search strategy for the high mass range includes either a direct search for the W or a search for evidence of b or $\bar{b}$ decay fragments in the event. The search for the W decay to jets will be difficult because of the poor mass resolution and the large QCD background of lepton+jets events. The CDF group hopes to employ soft muons from the b decay, or information from the recently installed silicon vertex detectors to help enhance the search. With these improvements to the apparatus, and the expected fivefold increase in the integrated luminosity, the sensitivity is expected to extend well above 120 GeV in top quark mass.

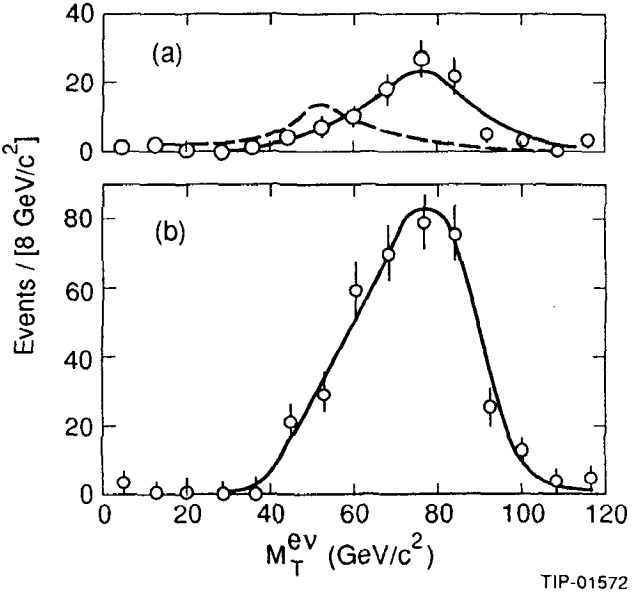

Figure 19 CDF results on (*a*) the transverse mass distribution for the electron + ≥ two-jet data (*points*), and predictions for W + two-jet (*solid curve*), and $t\bar{t}$ production with $M_{top} = 70$ GeV (*dashed curve*). (*b*) The measured transverse mass distribution for the electron + ≥ one-jet data together with W + one-jet prediction, normalized to equal number of events.

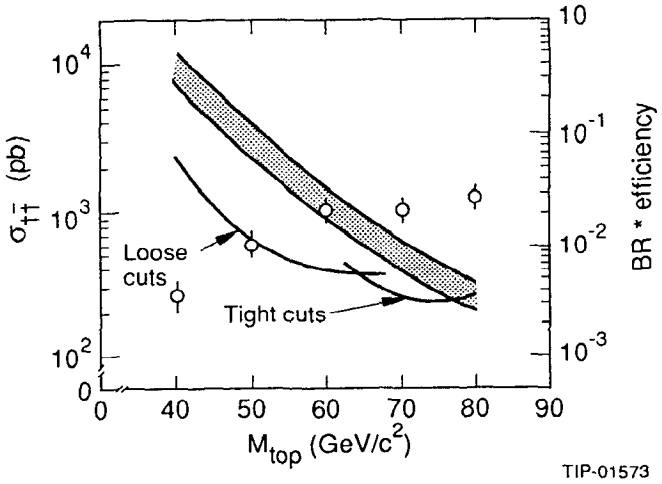

Figure 20 CDF results on the upper limit (95% confidence level) for the $t\bar{t}$ production cross section (*solid curve*). The predicted cross section is given by the shaded area. Plotted points show the $t\bar{t}$ branching ratio multiplied by the efficiency as a function of the top quark mass (*right-hand scale*).

6. SUPERSYMMETRIC STANDARD MODEL EXTENSIONS

Supersymmetric extensions of the Standard Model hypothesize an additional global symmetry that connects particles of differing spin (for a general review, see 54). The minimal model ($N = 1$ supersymmetry) has a single generator Q_x that transforms as spin-$\frac{1}{2}$ under the Lorentz group. Q_x acting on an ordinary massless state of helicity generates a superpartner of helicity $h-\frac{1}{2}$. Because of various commutation rules satisfied by Q_x, when Q_x is applied again, the result vanishes. For this reason, the supermultiplets are doublets, with two particles that differ by half a unit of spin angular momentum. The superparticles corresponding to the spin-1 gauge bosons are the spin-$\frac{1}{2}$ gauginos—gluino, wino, zino, and photino. The superparticles corresponding to the spin-$\frac{1}{2}$ fermions are spin-0 partners to the quarks and leptons named squarks and sleptons.

Since Q_x commutes with the other operators, the quantum numbers of the superpartners are the same as for the original particles, but they carry an additional quantum number R that is absolutely conserved. Since supersymmetry is not seen readily in nature, the symmetry must be broken. The conservation of R implies that the lightest superpartners must be stable. The expected scale of supersymmetric scale breaking should be of order M_W, so such particles might be expected to appear in the fragments of hadron-hadron collisions. In $p\bar{p}$ collisions, the gluinos ($\tilde{g}$) and squarks ($\tilde{q}$) are expected to be pair produced via QCD processes with a rather high rate.

In the simplest models, the photino ($\tilde{\gamma}$) is assumed to be the lightest superparticle and hence is stable. The decay modes for $m_{\tilde{q}} > m_{\tilde{g}}$ are $\tilde{q} \rightarrow \tilde{g}q$ and $\tilde{g} \rightarrow q\bar{q}\tilde{\gamma}$, and for $m_{\tilde{g}} > m_{\tilde{q}}$, they are $\tilde{g} \rightarrow \tilde{q}g$ and $\tilde{q} \rightarrow q\tilde{\gamma}$. The final states are composed of normal quarks and gluons, along with photinos. Since the photinos do not interact in the detector, the signature for supersymmetric (SUSY) particles is the production of some number of jets along with missing transverse momentum. The Standard Model backgrounds to this signature are dominated by the $\ell\nu$ decay mode of the W, and by Z+jet events, where the Z decays to $\nu\bar{\nu}$.

The CDF group has made a search for SUSY particles in the decay modes discussed above using a data sample of 25.3 nb^{-1}. To isolate events with the expected signature, events with $\not\!\!E_t > 30$ GeV and one cluster with $E_t > 15$ GeV are selected. The significance of the measured missing p_t (see Equation 16) is required to be above 2.8 to eliminate dijet fluctuations. This corresponds to roughly a 4σ cut on the $\not\!\!E_t$.

To further eliminate surviving dijet background, events containing two clusters with $E_t > 5$ GeV that are back to back in ϕ to within $\pm 30°$ are

removed from the sample. Cosmic rays are removed if more than 3 GeV of the energy are deposited out of time in the central hadron calorimeters. There are 115 events that survive these cuts. Since cosmic rays deposit large amounts of energy in the electromagnetic calorimeters where no timing information is available, the ratio of transverse momentum in tracks to the cluster transverse momentum is required to be above 0.2. In addition, to remove $W \rightarrow e\nu$ events, CDF requires that the leading cluster deposit at least 10% of its energy in the hadron calorimeter. After correcting the missing p_t for the presence of tracks passing through cracks in the calorimetry, two events remain. They have $\not{E}_t = 35.2$ and 36.1 GeV.

To set a limit on SUSY particle production, the systematic errors on the luminosity, event selection, and jet energy scale are taken into account. Limits are set using the most conservative set of structure functions, namely those that give the weakest limit. Figure 21 shows the result along with limits from UA1 and UA2. The discontinuity along the line $m_{\tilde{q}} = m_{\tilde{g}}$ is due to the differing acceptances for the allowed decay modes. Searches

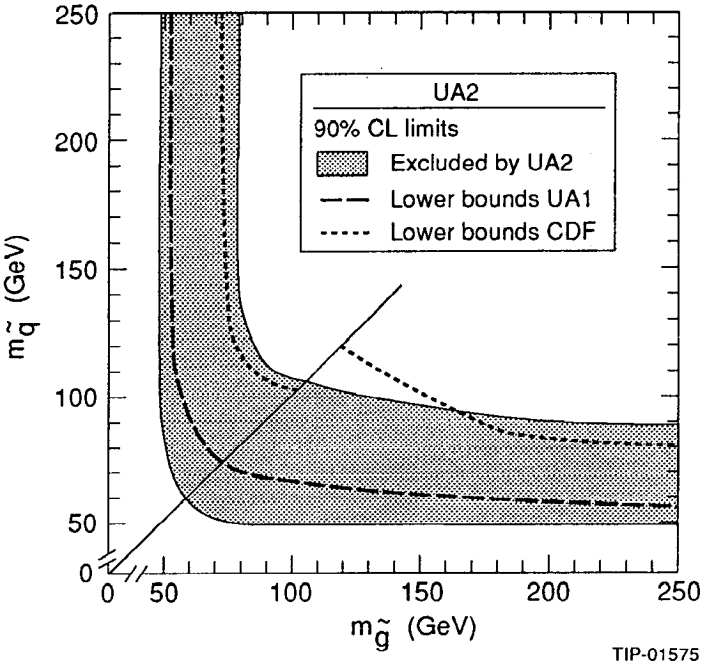

Figure 21 The 90% confidence level excluded region in the $m_{\tilde{q}}$ and $m_{\tilde{g}}$ plane, as measured by the UA1, UA2, and CDF collaborations.

made in the latest data samples thus far show no evidence for SUSY particle production.

7. CONCLUSIONS

Experience with multipurpose detectors at hadron-hadron colliders is growing rapidly. The calculability of the event rates for known and hypothetical processes makes hadron-hadron colliders an interesting laboratory for both new particle searches and precision parameter measurements. This review focused mainly on measurements of particles and processes predicted by the Standard Model. A wealth of recent results shows that these detectors are also sensitive to non–Standard Model physics (53). So far, all results are in agreement with Standard Model predictions. Large data sets should be collected by the CDF and D0 experiments in the near future and should provide a wealth of new information, especially on heavy flavor (bottom and top quark) production.

Literature Cited

1. Abramovskii, V. A., Kanchelli, O. V., Gribov, V. N., In *Proc. 16th Int. Conf. on High Energy Physics*, ed. J. D. Jackson, A. Roberts. Batavia, Ill: Fermi Natl. Lab. (1972), I: 363
2. Feynman, R. P., *Photon-Hadron Interactions*. Reading, Mass: Benjamin (1972); Berman, S. M., Jacob, M., *Phys. Rev. Lett.* 25: 1683 (1970); Berman, S. M., Bjorken, J. D., Kogut, J. B., *Phys. Rev.* D4: 3388 (1971)
3. Altarelli, G., *Phys. Rev.* 81C: 1 (1982)
4. Altarelli, G., et al., *Nucl. Phys.* B143: 521 (1978); Erratum, *Nucl. Phys.* B146: 544 (1978)
5. Aurenche, P., et al., *Phys. Lett.* B169: 441 (1986); B140: 87 (1984)
6. Dawson, S., Ellis, R. K., Nason, P., *Nucl. Phys.* B303: 607 (1988)
7. Ellis, R. K., Sexton, J. C., *Nucl. Phys.* B269: 445 (1986); Ellis, S. D., Kunszt, Z., Soper, D., Zurich preprint ETH-TH/90-3 (1990)
8. UA1 Collaboration, *Nucl. Instrum. Methods* B147: 392 (1984); *Phys. Scr.* 23: 397 (1981)
9. Beer, A., et al., *Nucl. Instrum. Methods* 224: 360 (1984)
10. Abe, F., et al., *Nucl. Instrum. Methods* 271: 487 (1988)
11. D0 Collaboration, *D0 Design Report*. Batavia, Ill: Fermi Natl. Lab. (1983)
12. Hinchliffe, I., Shapiro, M., *Rep. QCD Working Group*, in *Proc. Summer Study on High Energy Physics in the 1990's*, ed. S. Jensen. Singapore: World Scientific (1989)
13. Banner, M., et al., *Phys. Lett.* B118: 203 (1982)
14. Schwitters, R., in *Proc. 1983 SLAC Summer Inst.*, SLAC Rep. No. 267, ed. P. McDonough. Stanford, Calif: SLAC (1983)
15. Arnison, G., et al., *Phys. Lett.* B118: 185 (1982)
16. Abe, F., et al., *Phys. Rev. Lett.* 62: 613 (1989)
17. Ellis, S. D., et al., See Ref. 7
18. Owens, J. F., *Rev. Mod. Phys.* 59: 465 (1987)
19. Eichten, E., Lane, K., Peskin, M., *Phys. Rev. Lett.* 50: 811 (1983)
20. Hessing, T. L., for the CDF Collaboration see Ref. 50
21. UA2 Collaboration, CERN preprint CERN-EP/90-188 (1990); *Phys. Lett.* B257: 232 (1991)
22. UA2 Collaboration, *Z. Phys.* C30: 341 (1986)
23. UA1 Collaboration, *Phys. Lett.* B158: 494 (1985)
24. Berends, F. A., et al., *Phys. Lett.* B103: 124 (1982)
25. Appel, J., et al., *Z. Phys.* C30: 341 (1986)
26. Plunkett, R., for the CDF Collaboration, Jet Dynamics at the Tevatron Col-

lider, in *Proc. 8th Topical Workshop on Proton-Antiproton Collider Physics*. Castiglione Della Pescaia, Italy. Singapore: World Scientific (1989)
27. Abe, F., et al., *Nucl. Instrum. Methods* A271: 387 (1988); *Phys. Rev. Lett.* 62: 1005 (1989)
28. UA2 Collaboration, *Z. Phys.* C47: 11 (1990); Ansorge et al., *Nucl. Instrum. Methods* A265: 33 (1988)
29. UA1 Collaboration, *Phys. Lett.* B186: 237 (1987); *Z. Phys.* C37: 505 (1988)
30. Deleted in proof
31. UA2 Collaboration, *Phys. Lett.* B186: 152 (1987)
32. Amaldi, U., et al., *Phys. Rev.* D36: 1385 (1987); Kennedy, D. C., Langacker, P., *Phys. Rev. Lett.* 65: 2967 (1990); Altarelli, G., Barbieri, R., CERN TH.5863/90 (1990)
33. Yamaguchi, Y., *Nuovo Cimento* A43: 193 (1966); Drell, S. D., Yan, T. M., *Phys. Rev. Lett.* 25: 316 (1970)
34. Altarelli, G., et al., *Nucl. Phys.* B246: 12 (1984); Altarelli, G., Ellis, K., Martinelli, G., *Z. Phys.* C27: 617 (1985)
35. Altarelli, G., et al., *Phys. Rev. Lett.* 63: 720 (1989); Arnold, P. B., Kauffman, R. P., ANL-HEP-PR-90-70; *Nucl. Phys. B*. In press (1991)
36. UA2 Collaboration, *Z. Phys.* C47: 11 (1990); Abe, F., et al., *Phys. Rev. Lett.* 62: 1005 (1989)
37. UA2 Collaboration, *Z. Phys.* C47: 523 (1990)
38. Abe, F., et al., *Phys. Rev. Lett.* 65: 2243 (1990)
39. UA2 Collaboration, *Phys. Lett.* B241: 150 (1990)
40. Abe, F., et al. *Phys. Rev. Lett.* 63: 720 (1989)
41. Particle Data Group, *Phys. Lett.* B239, Vol. 2 (1990)
42. Abe, F., et al., Fermilab PUB-90-229-E, *Phys. Rev. D*. In press (1991)
43. Abe, F., et al., *Phys. Rev. Lett.* 64: 152 (1990)
44. ALEPH Collaboration, *Phys. Lett.* B236: 511 (1990)
45. UA1 Collaboration, see Ref. 29
46. Baden, D., for the CDF Collaboration, *B Physics at CDF*, in *Proc. SLAC Summer School Topical Conf. on Gauge Bosons and Heavy Quarks*, ed. E. Brennan. Stanford, Calif: SLAC (1990)
47. Kennedy, D. C., Langacker, P., See Ref. 32
48. Dawson, S., et al., See Ref. 6
49. Abe, F., *Phys. Rev. Lett.* 64: 147 (1990)
50. Sliwa, K., for the CDF Collaboration, *Proc. 25th Rencontre de Moriond*, ed. J. Tran Thanh Van. Savoie, France: Les Arcs (1990)
51. UA2 Collaboration, *Z. Phys.* C46: 179 (1990)
52. Abe, F., *Phys. Rev. Lett.* 64: 142 (1990)
53. UA2 Collaboration, *Phys. Lett.* B235: 363 (1990); UA2 Collaboration, *Phys. Lett.* B238: 442 (1990); Abe, F., et al., *Phys. Rev. Lett.* 62: 1825 (1989)
54. Hinchliffe, I., *Annu. Rev. Nucl. Part. Sci.* 36: 505–43 (1986)
55. Alner, C. G., et al., *Phys. Rev.* 154: 247 (1987)
56. Abe, F., et al., *Phys. Rev. Lett.* 61: 1819 (1988)
57. Arnison, G., et al., *Phys. Lett.* B118: 167 (1982)
58. Alper, B., et al., *Nucl. Phys.* B87: 19 (1975)
59. Anreasyan, D., et al., *Phys. Rev.* D19: 764 (1979)

Annual Review of Nuclear and Particle Science
Volume 41, 1991

CONTENTS